

Resonant inelastic X-ray scattering determination of the electronic structure of oxyhemoglobin and its model complex

James J. Yan^a, Thomas Kroll^{a,b}, Michael L. Baker^a, Samuel A. Wilson^a, Richard Decréau^{a,c}, Marcus Lundberg^{a,d}, Dimosthenis Sokaras^b, Pieter Glatzel^e, Britt Hedman^{b,1}, Keith O. Hodgson^{a,b,1}, and Edward I. Solomon^{a,b,1}

^aDepartment of Chemistry, Stanford University, Stanford, CA 94305; ^bStanford Synchrotron Radiation Lightsource, SLAC National Accelerator Laboratory, Stanford University, Menlo Park, CA 94025; ^cInstitut de Chimie Moléculaire de l'Université de Bourgogne - CNRS UMR 6302, University Bourgogne Franche Comté, 21078 Dijon, France; ^dDepartment of Chemistry - Ångström Laboratory, Uppsala University, SE-751 21 Uppsala, Sweden; and ^eEuropean Synchrotron Radiation Facility, 38043 Grenoble, Cedex 9, France

Edited by Michael L. Klein, Institute of Computational Molecular Science, Temple University, Philadelphia, PA, and approved December 28, 2018 (received for review September 17, 2018)

Hemoglobin and myoglobin are oxygen-binding proteins with $S = 0$ heme $\{\text{FeO}_2\}^8$ active sites. The electronic structure of these sites has been the subject of much debate. This study utilizes Fe K-edge X-ray absorption spectroscopy (XAS) and 1s2p resonant inelastic X-ray scattering (RIXS) to study oxyhemoglobin and a related heme $\{\text{FeO}_2\}^8$ model compound, $[(\text{pfp})\text{Fe}(\text{1-MeIm})(\text{O}_2)]$ (pfp = meso-tetra($\alpha,\alpha,\alpha,\alpha$ -*o*-pivalamido-phenyl)porphyrin, or TpvPP, 1-MeIm = 1-methylimidazole) (pfpO₂), which was previously analyzed using L-edge XAS. The K-edge XAS and RIXS data of pfpO₂ and oxyhemoglobin are compared with the data for low-spin Fe^{II} and Fe^{III} $[\text{Fe}(\text{tpp})(\text{Im})_2]^{0/+}$ (tpp = tetra-phenyl porphyrin) compounds, which serve as heme references. The X-ray data show that pfpO₂ is similar to Fe^{II}, while oxyhemoglobin is qualitatively similar to Fe^{III}, but with significant quantitative differences. Density-functional theory (DFT) calculations show that the difference between pfpO₂ and oxyhemoglobin is due to a distal histidine H bond to O₂ and the less hydrophobic environment in the protein, which lead to more back-bonding into the O₂. A valence bond configuration interaction multiplet model is used to analyze the RIXS data and show that pfpO₂ is dominantly Fe^{II} with 6–8% Fe^{III} character, while oxyhemoglobin has a very mixed wave function that has 50–77% Fe^{III} character and a partially polarized Fe–O₂ π -bond.

X-ray spectroscopy | resonant inelastic X-ray scattering | DFT | oxyhemoglobin | electronic structure

The electronic structure of the active sites in oxyhemoglobin (HbO₂) and oxymyoglobin has been the subject of study and debate for decades. The iron oxygen-binding proteins contain an $S = 0$ $\{\text{FeO}_2\}^8$ active site, denoting eight valence electrons delocalized among the Fe 3d and O₂ π^* -orbitals in the Enemark–Feltham (1) notation used for metal–NO complexes. Three electronic structure models have been proposed by Pauling and Coryell (2, 3) (low-spin Fe^{II} with singlet O₂), Weiss (4) (low-spin Fe^{III} antiferromagnetically coupled to doublet O₂[−]), and McClure (5), Harcourt (6, 7), and Goddard and Olafson (8) ($S = 1$ Fe^{II} antiferromagnetically coupled to triplet O₂, also known as the “ozone” model). Much computational work has been done, with all three models supported by different calculations (9–13). However, there has been a dearth of experimental data to directly probe the electronic structure. In particular, the intense porphyrin $\pi \rightarrow \pi^*$ transitions of heme complexes make it difficult to probe the highly covalent Fe with traditional spectroscopic methods (14, 15).

X-ray absorption spectroscopy (XAS), a site-specific technique that provides a direct probe of the metal center, has added to the controversy. An analysis of the iron K preedge suggested that HbO₂ has an electronic structure similar to the Weiss model in solution, but that crystalline HbO₂ has an electronic structure more similar to the Pauling model (16). Alternatively, a recent X-ray emission K β study suggested that the iron center has an $S = 1$ Fe^{II} spin state,

similar to the ozone model (17). However, neither technique provides a quantitative analysis of the electronic structure of iron centers. In contrast, L-edge XAS measures the electric-dipole-allowed metal 2p \rightarrow 3d transitions, where the integrated intensity is proportional to the total amount of metal 3d character in the valence orbitals (18). This makes the technique powerful in studying highly covalent metal sites. Quantitative covalency information can be extracted through modeling of the L-edge XAS spectra using a valence bond configuration interaction (VBCI) multiplet model (19). This methodology has been applied to iron complexes to extract the differential orbital covalency (DOC), which allows for quantification of ligand σ - and π -donation (18, 20, 21) and metal π -backbonding (22), including in heme models (14).

L-edge XAS and the VBCI multiplet model were used to analyze the $S = 0$ $\{\text{FeO}_2\}^8$ heme model compound $[(\text{pfp})\text{Fe}(\text{1-MeIm})(\text{O}_2)]$ [pfp = meso-tetra($\alpha,\alpha,\alpha,\alpha$ -*o*-pivalamido-phenyl)porphyrin, 1-MeIm = 1-methylimidazole] (pfpO₂) (23). That study determined that the pfpO₂ model compound had an electronic structure more similar to the Pauling model. The pfpO₂ compound has been seen as a good model for HbO₂, with similar vibrational (24–27) and Mössbauer spectra (28–33). One major difference between the model complex and the protein is that the protein has a conserved histidine in the active site that can hydrogen-bond to the O₂. This hydrogen bond has been calculated

Significance

The electronic structure of the heme oxy-iron center in oxyhemoglobin and oxymyoglobin has been the subject of debate for decades. Various experimental and computational methods have been used to study this system, leading to conflicting conclusions. This study uses X-ray spectroscopy to directly probe the iron center in the highly delocalized oxyhemoglobin and its model compound to define the electronic structure and understand the differences between the protein and the model. This study settles a longstanding debate in bioinorganic chemistry and provides insight into heme iron–oxygen binding, the key first step in many biocatalytic processes.

Author contributions: J.J.Y., B.H., K.O.H., and E.I.S. designed research; J.J.Y., T.K., S.A.W., R.D., M.L., D.S., and P.G. performed research; M.L.B. contributed new reagents/analytic tools; J.J.Y. and T.K. analyzed data; and J.J.Y., B.H., K.O.H., and E.I.S. wrote the paper.

The authors declare no conflict of interest.

¹To whom correspondence may be addressed. Email: hedman@slac.stanford.edu, HodgsonK@stanford.edu, or edward.solomon@stanford.edu.

Published online February 4, 2019.

by Shaik and coworkers (9) to be important in modulating the electronic structure of oxymyoglobin, leading to a more polarized Weiss-like description. It is therefore important to experimentally compare the pfpO₂ model compound with the HbO₂ protein.

One major limitation of iron L-edge XAS is that it occurs in the soft X-ray regime (~710 eV), which requires ultrahigh vacuum that limits the measurement of protein or solution samples. However, “L-edge-like” information can be obtained through 1s2p resonant inelastic X-ray scattering (RIXS) (34). The 1s2p RIXS involves a two-step process, where a hard (~7,100-eV) X-ray incident photon of energy Ω causes a 1s \rightarrow 3d transition, followed by 2p \rightarrow 1s decay, releasing a photon of energy ω (35, 36). The resulting 2p³3dⁿ⁺¹ final-state configuration is the same as for L-edge XAS, which can be simulated with the VBCI multiplet model to extract the DOC and provide a quantitative bonding description (37). The 1s2p RIXS can therefore be used to directly compare protein and model compounds. It is a complementary technique to L-edge XAS and the differences between L-edge XAS and 1s2p RIXS have been previously studied with several nonheme iron model compounds (38).

A combined L-edge XAS and 1s2p RIXS methodology was developed and applied to study the bonding in ferrous and ferric cytochrome *c* (39). This involved an initial analysis of heme model compounds that could be measured by both L-edge XAS and 1s2p RIXS, which allowed for calibration of the VBCI model between the two techniques. The 1s2p RIXS analysis of the model compound was then used to calibrate the 1s2p RIXS analysis of the protein system, where L-edge XAS data were unavailable. This methodology is applied in the present study, by first studying the 1s2p RIXS of pfpO₂, for which the L-edge XAS analysis has been done, and then using this model as a reference for the analysis of the 1s2p RIXS of HbO₂.

Results and Analysis

RIXS Planes. The two-dimensional background-subtracted RIXS data for both pfpO₂ and HbO₂ are shown in Fig. 1 B and C, respectively, along with the RIXS planes of [Fe^{II}(tpp)(ImH)₂] (Fe2tpp, Fig. 1A) and [Fe^{III}(tpp)(ImH)₂]⁺ (Fe3tpp, Fig. 1D) included as references for low-spin Fe^{II} and low-spin Fe^{III} in porphyrin environments (large version in *SI Appendix*, Fig. S1). The RIXS planes for pfpO₂ and HbO₂ exhibit clear differences. The pfpO₂ plane has only a single incident energy resonance (*x* axis) at 7,112.2 eV. The main L₃ feature of the resonance is broad along the energy transfer direction ($\Omega - \omega$, *y* axis) and resolves into two peaks, with the main peak at 707.2 eV and an intense shoulder at 708.3 eV. At higher energy, a low-intensity satellite feature also appears at ~710 eV. The pattern of the RIXS plane of pfpO₂, with a single incident energy resonance and a double-peak feature in the energy transfer direction, is very similar to the pattern of the RIXS plane of Fe2tpp (Fig. 1A).

Unlike pfpO₂, HbO₂ clearly shows two incident energy resonances, with a small, weak feature at 7,111.4 eV, and a large, broad feature at 7,112.8 eV. The 7,112.8-eV resonance does not exhibit the double-peak feature seen in the pfpO₂ and Fe2tpp planes. The HbO₂ RIXS plane is not only different from the low-spin Fe^{II} reference plane, but is also very different from the low-spin Fe^{III} reference plane (Fig. 1D). The “d π ”-resonance (7,111.3 eV) in the Fe3tpp plane is higher in intensity than the low-energy resonance in HbO₂ and is also further separated in energy from the main peak (7,112.9 eV) in the energy transfer direction. For Fe3tpp, the low-energy peak of the L₃ occurs at 706 eV in the energy transfer direction, with the main peak at 708 eV, compared with 706.5 and 708 eV, respectively, in HbO₂. From the comparison of the RIXS planes, pfpO₂ experimentally appears very similar to Fe2tpp, while HbO₂ appears more “ferric-like” than pfpO₂, but significantly less than Fe3tpp.

Constant Emission Energy Cuts and K-Edge Spectroscopy. The K-edge spectra of pfpO₂ and HbO₂ are shown in Fig. 2 B and C,

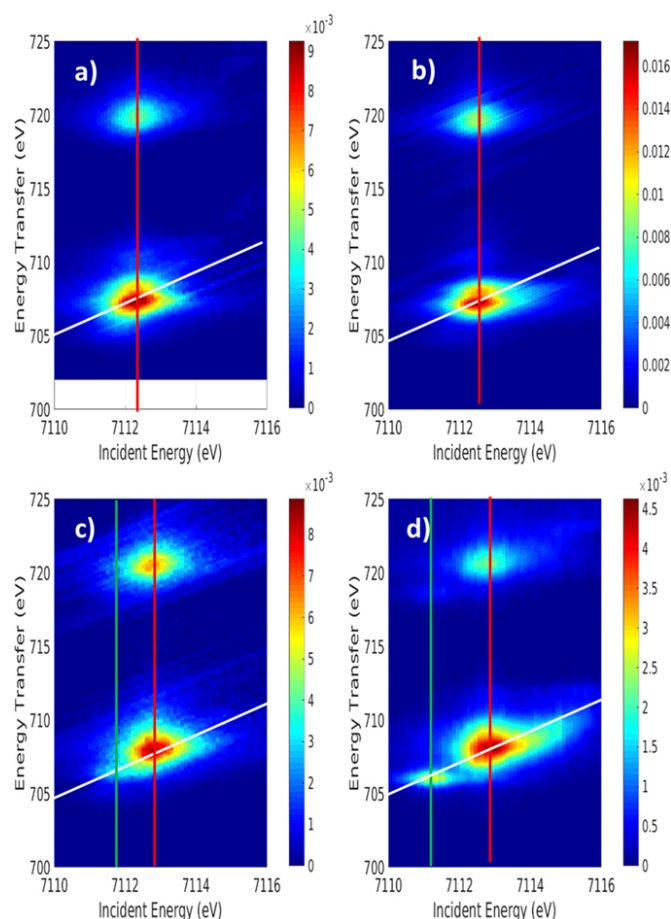


Fig. 1. Background-subtracted RIXS planes of (A) Fe2tpp, (B) pfpO₂, (C) HbO₂, and (D) Fe3tpp. The diagonal white lines represent where CEE cuts were made. The vertical red and green lines represent where CIE cuts were made.

along with comparisons to the corresponding constant emission energy (CEE) cuts (full K-edge X-ray absorption near edge structure in *SI Appendix*, Fig. S2). The CEE cuts were made through the maxima of the RIXS planes and are marked by the diagonal white lines through the planes in Fig. 1. The integrated intensity of the pfpO₂ preedge is 4.1 units, while the HbO₂ preedge is more intense at 6.7 units. The pfpO₂ preedge intensity is comparable to the preedge intensities of other six-coordinate low-spin ferrous and ferric compounds (three to five units) (40), including Fe2tpp (4.9) and Fe3tpp (4.3). While HbO₂ has a more intense preedge than the other compounds, it is still significantly lower in intensity than the preedge intensities of distorted six-coordinate protein active sites (~8 units) (41) and of four-coordinate tetrahedral and square pyramidal five-coordinate compounds (11+ units). The latter have significant electric-dipole intensity due to 4p mixing caused by loss of inversion symmetry (40). This means that the preedge features of pfpO₂ are primarily due to 1s \rightarrow 3d quadrupole excitations, but HbO₂ has a small amount of dipole intensity due to limited distortion at the Fe center.

In comparing the K edges with the CEE cuts in Fig. 2 B and C, the main insight is that the CEE cuts in red and green provide a higher-energy-resolution K edge. In the CEE cut of pfpO₂, there is a single preedge peak, as in the K edge, but with a higher energy shoulder. This shoulder is not due to a new 1s \rightarrow 3d excitation, but is due to overlap with the feature in the preedge that occurs at the same incident energy, but higher energy transfer in Fig. 1B. This phenomenon was noted in our previous RIXS studies and emphasizes the need to collect the full 2D RIXS plane to analyze these data (38).

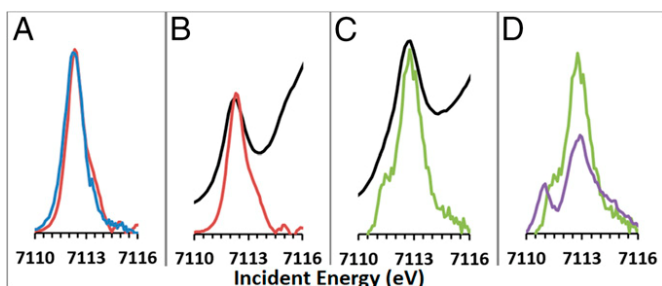


Fig. 2. (A) Comparison of CEE cut of pfpO₂ (red) with Fe2tpp (blue). (B) Comparison of K-edge spectrum of pfpO₂ (black) with CEE cut (red). (C) Comparison of K-edge spectrum of HbO₂ (black) with CEE cut (green). (D) Comparison of CEE cut of HbO₂ (green) with Fe3tpp (purple).

The high-resolution CEE cut of HbO₂ clearly shows two peaks, with a small peak at lower incident energy (Fig. 2C). This peak is much less clear in the K edge, where analysis of the second derivative is necessary to confirm the presence of the peak. The CEE cuts emphasize the differences between pfpO₂ and HbO₂ seen in the RIXS planes. To compare cuts between the different samples, cuts were scaled such that the RIXS pre-edge integrated intensity was the same as that obtained through K-edge XAS. The pfpO₂ CEE cut is very similar to the CEE cut of Fe2tpp (Fig. 2A). The HbO₂ CEE cut is very different from that of Fe3tpp (Fig. 2D). While the lower-energy peak appears comparable in intensity to that in Fe3tpp, the energy splitting between the low-energy peak and the main peak is much smaller. The main peak in HbO₂ is also much more intense than in Fe3tpp. From the crystal structures of HbO₂, the Fe–O₂ bond length is ~1.8 Å, compared with ~2 Å for the other bonds (42). This would lead to 4p_z mixing with d_{2z}, which would increase the intensity in the main peak (40). Although HbO₂ displays two peaks in its CEE cut, it has significant and quantitative differences from the low-spin ferric reference spectrum.

Constant Incident Energy Cuts and L-Edge Spectroscopy. The L-edge spectrum of pfpO₂ was analyzed in a previous study (23) and is compared with the constant incident energy (CIE) cut through the maximum of the RIXS preedge in Fig. 3. The CIE is given by the red vertical lines in Fig. 1. Unlike the L-edge spectrum (dotted), which has one prominent peak in the L₃ region, the CIE cut has a broad double peak, with the lower-energy peak being higher in intensity. The higher-energy satellite feature, at ~710 eV, is higher in intensity in the L-edge spectrum compared with the CIE cut. The L₂ region of the CIE cut is also higher in intensity compared with the L-edge spectrum. Fig. 3 (Inset) shows a comparison of the CIE cut of pfpO₂ with the CIE cut of Fe2tpp. The cuts are qualitatively very similar, with both showing a broad double-peak main feature in the L₃ region. There are however several notable differences between the two cuts, with the pfpO₂ cut having less intensity in the region at ~707.5 eV and in the higher-energy satellite feature at ~710 eV, but more intensity in the L₂ region (~720 eV), compared with the Fe2tpp cut. These differences are very similar to those previously observed comparing Fe2tpp to reduced cytochrome *c*, where there is also a change in the axial ligation (N to S) (39).

For HbO₂, there is no comparison between L-edge and RIXS CIE cuts, due to the limitations in acquiring L-edge spectra on proteins. The comparison of the CIE cuts through the maxima of the two resonances in HbO₂ (given by the vertical lines in Fig. 1C) with the CIE cuts through the maxima of the two resonances in Fe3tpp is shown in Fig. 4. The most significant difference between the two datasets comes from the CIE cut through the low-energy dπ-peak (green). While the Fe3tpp cut (dotted) has a sharp, intense peak at 706 eV with some residual intensity from the main

resonance at 708 eV, the HbO₂ cut (solid) has a lower-intensity peak at 706.5 eV that is barely discernible from the residual intensity from the main resonance. In the CEE, the low-energy peaks appear comparable in intensity, but the CIE cuts clearly show that the HbO₂ peak has lower intensity compared with Fe3tpp and has a smaller energy splitting between the low-energy peak and the main peak. The cuts through the main peak show similar shapes, but with HbO₂ having higher intensity due to the dipole contribution (*vide supra*).

Thus, the RIXS data show significant differences between HbO₂ and pfpO₂. pfpO₂ has spectral features qualitatively like that of the low-spin ferrous reference compound, while HbO₂ has two incident energy resonances, similar to that of the low-spin ferric reference compound. However, the HbO₂ spectrum has significant quantitative differences in peak energy and intensity compared with the Fe3tpp spectrum. The next section uses DFT calculations to gain insight into the origin of these differences. The electronic structures of pfpO₂ and HbO₂ are analyzed further with VBCI modeling of these different RIXS planes in the last section of the analysis.

DFT Calculations. The RIXS data show significant differences between the electronic structures of HbO₂ and pfpO₂. To understand the source of these differences, DFT calculations were performed on these systems using the crystal structures as the starting geometries (42, 43), with toluene as the solvent in a polarized continuum model for pfpO₂. For HbO₂, the proximal histidine, which binds directly to the Fe, as well as the distal histidine, which can H-bond with the O₂ and has been implicated in tuning the electronic structure of the site (9), were included in the calculation as full amino acid residues (*SI Appendix*, Fig. S3). Additionally, a side-chain carbonyl that may H-bond with the proximal histidine was modeled using a formaldehyde (16), and a dielectric of 10 was used to model the protein environment. Geometry optimizations were performed on the starting structures using the BP86 functional. Single-point calculations with B3LYP and BP86 gave similar results (*SI Appendix*, Figs. S4 and S5). In all cases, a polarized electronic structure was found lowest in energy by a few kilocalories per mole. Full computational details can be found in *SI Appendix*, *SI Materials and Methods*.

The electronic structure results of the calculations are given in Table 1 and *SI Appendix*, Fig. S5 and Table S1, along with calculations on Fe2tpp and Fe3tpp as reference compounds. The optimized structures of pfpO₂ and HbO₂ have very similar coordination environments around the Fe. The calculated

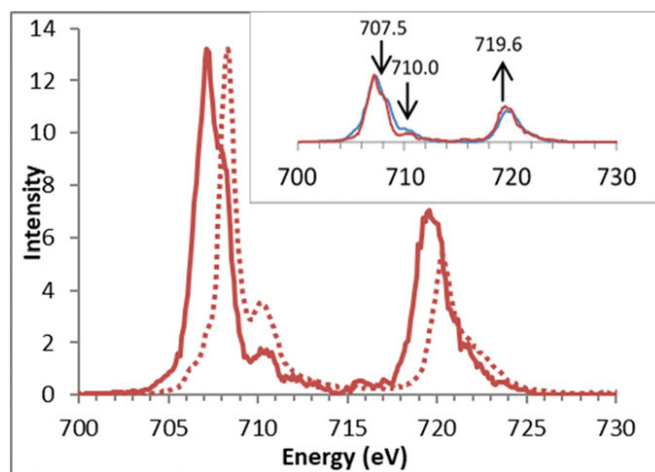


Fig. 3. The CIE cut of pfpO₂ at 7,112.2 eV (solid) with the L-edge spectrum (dotted). (Inset) Comparison of the CIE cut of pfpO₂ (red) with Fe2tpp (blue). Arrows show where pfpO₂ has different intensity from that of Fe2tpp.

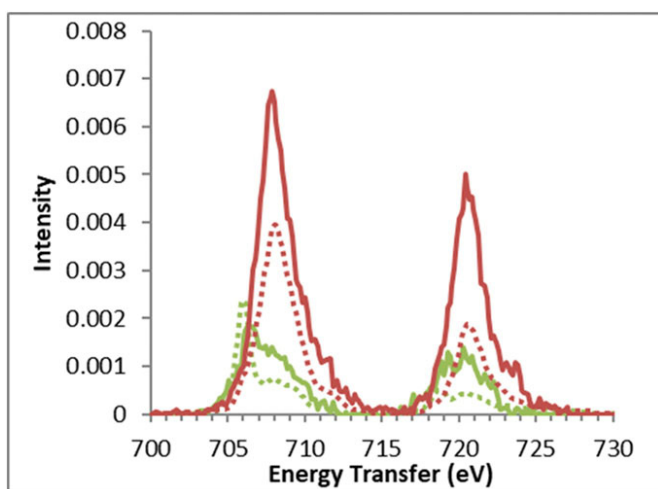


Fig. 4. Comparison of CIE cuts of HbO₂ (solid) and Fe3tp (dotted). CIE cuts through the low-energy peaks (at 7,111.4 eV for HbO₂ and 7,111.3 eV for Fe3tp) are in green. CIE cuts through the main peaks (at 7,112.8 eV for HbO₂ and 7,112.9 eV for Fe3tp) are in red. The CIE cuts are scaled to match the RIXS and K preedge integrated intensities.

electronic structures are also largely similar, with both having ~344% total unoccupied metal 3d character in the valence orbitals (Table 1). This is to be compared with 346 and 313% for the Fe3tp and Fe2tp references, respectively. Thus, both are calculated to be closer to Fe^{III}; however, the experimental L-edge XAS total d character for pfpO₂ is closer to Fe^{II}. The main difference is found in the backbonding. While the total amount of backbonding of occupied Fe character into the porphyrin and O₂ π* (Table 1) orbitals is the same for both complexes (~93%, Table 1), the distribution of this metal character is different. pfpO₂ has less backbonding into the O₂ π* (68.8 vs. 76.2%), which is compensated by increased backbonding into the porphyrin π*-orbitals. This difference in Fe–O₂ bonding explains the slightly longer Fe–O (1.83 vs. 1.82 Å) and shorter O–O (1.30 vs. 1.32 Å) calculated bonds in pfpO₂ compared with HbO₂ (SI Appendix, Table S1).

Based on the models used for the calculation, this difference in backbonding can be due to several factors: (i) the carbonyl H bond to the proximal histidine, (ii) the dielectric, (iii) the distal histidine H bond to the O₂, and/or (iv) the different porphyrins (heme b vs. picket-fence porphyrin). These factors were investigated through perturbations to the HbO₂ model (SI Appendix, Fig. S6). Removing the carbonyl H bond to the proximal histidine in the calculation showed minimal effect (76.2 vs. 76.1%

backbonding to O₂) on the electronic structure, in contrast to previous calculations (16). Then lowering the dielectric constant from 10 (protein) to 2.4 (toluene) decreased the backbonding to O₂ from 76.1 to 74.3%, while subsequent removal of the distal histidine further lowered the backbonding to 69.1%, similar to pfpO₂. The latter effect has been described by Shaik and coworkers (9). Since this perturbed heme b model has the same bonding description as in pfp, these calculations show that this difference in porphyrin has minimal effect on the electronic structure, the primary effect coming from the distal histidine H bond to O₂, and the less hydrophobic environment of the protein pocket.

The difference in backbonding to the O₂ qualitatively explains the spectral differences between pfpO₂ and HbO₂ in the RIXS data. As seen in the VBCI modeling (*vide infra*), increased backbonding from the Fe into the O₂ leads to a more polarized electronic structure associated with the appearance of the low-energy feature seen in the HbO₂ RIXS plane. In comparing the pfpO₂ and HbO₂ calculations with those of Fe2tp and Fe3tp, both are more like Fe3tp than Fe2tp (SI Appendix, Fig. S5, Right and Left, respectively). The π-bonding into O₂ leads to a low-energy α-hole with significant metal character (~63%), like the dπ-hole in Fe3tp (70.9%) (purple orbital α1 in SI Appendix, Fig. S5). The total unoccupied metal 3d character is also very close to that of Fe3tp (346.2%), but not Fe2tp (313.2%). This significantly contrasts the experimental XAS and RIXS data, which show that pfpO₂ is more like Fe2tp, and that HbO₂, while having a preedge feature associated with spin polarization, is still significantly different from Fe3tp (*vide supra*). Time-dependent-DFT calculations were also performed, which also show that the HbO₂ and pfpO₂ calculations are more ferric-like than seen experimentally (SI Appendix, SI TD-DFT Analysis).

VBCI Modeling. Since the DFT calculations provide a spin-polarized electronic structure description for both pfpO₂ and HbO₂ that have more ferric character than the experimental data suggest, a semiempirical VBCI multiplet model was used to fit the RIXS data to lock in on the electronic structure of the two compounds. The VBCI model provides a quantitative measure of the DOC in a metal complex by mixing the ground 3dⁿ configuration with ligand-to-metal charge transfer (LMCT) (3dⁿ⁺¹L̄, L̄ = ligand hole) and metal-to-ligand charge transfer (MLCT) (3dⁿ⁻¹L̄) configurations. The weight of the configurations in the mixed wave function depends on the relative energy of the configurations (Δ) and the strength of the mixing (T).

Previous studies have shown that by varying the weights of the charge-transfer configurations, it is possible to simulate ferrous (and ferric) L-edge spectra using both a ferric and a ferrous ground configuration (22, 23). This approach can be applied to

Table 1. Amount of metal 3d character in the lowest unoccupied orbitals calculated using the BP86 functional with experimental values in parentheses

Compound	Calculated % Metal 3d Character in Unoccupied Orbitals										
	σ, d _z ²		σ, d _{x²-y²} /x		π*, por [†]		π*, O ₂		Total [‡]	Total backbonding [§]	O ₂ backbonding
	α	β	α	β	α	β	α	β			
Fe2tp	66.5	66.5	71.2	71.2	9.5	9.5	N/A	N/A	313.2 (302)	37.8	N/A
pfpO ₂	63.2	55.5	68.6	64.1	9.5	2.9	59.8	9.0	344.9 (310)	93.5	68.8
HbO ₂	61.3	56.7	68.1	63.6	6.1	2.3	64.4	11.8	342.7	93	76.2
Fe3tp	66.5	63.3	67.2	62.8	5.7	2.1	70.9 [¶]	N/A	346.2 (365)	18.6	N/A

For Fe2tp, the closed-shell solution was lowest in energy so α- and β-occupancies are the same

[†]The metal values for the porphyrin π*-orbitals are an average of two different orbitals.

[‡]Experimental unoccupied 3d character comes from L-edge integrated intensity, which does not exist for HbO₂.

[§]Total backbonding includes backbonding to both O₂ and porphyrin π*-orbitals and is the sum of metal character from the orbitals.

[¶]This value for Fe3tp represents the metal character in the dπ-hole.

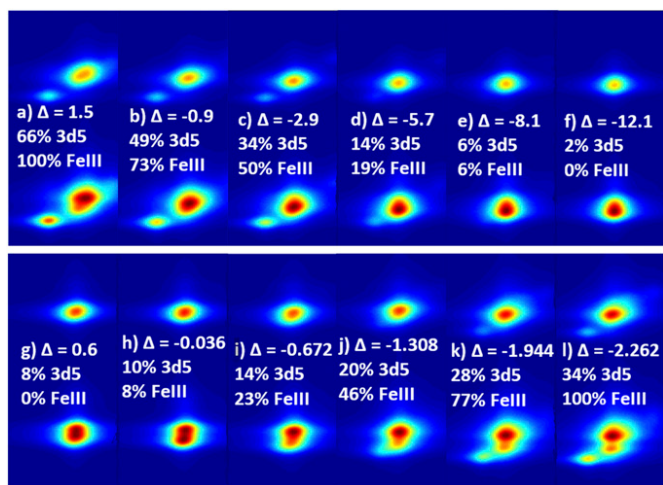


Fig. 5. (Top) VBCI RIXS simulations progressing from Fe^{III} → Fe^{II} using the ferric 3d⁵ ground configuration, starting with the fit for Fe3tpp in A, with fits for HbO₂ (C), pfpO₂ (E), and Fe2tpp (F). In this series, Δ is decreased from 1.5 in A, to -12.1 in F, decreasing the weight of the 3d⁵ configuration and becoming dominantly 3d⁶. (Bottom) VBCI RIXS simulations progressing from Fe^{II} → Fe^{III} using the ferrous 3d⁶ ground configuration, starting with the fit for Fe2tpp in G, with fits for pfpO₂ (H), HbO₂ (K), and Fe3tpp (L). Full fit parameters for Fe2tpp and Fe3tpp can be found in *SI Appendix*, Table S2. In this series, Δ_{bb} is decreased from 0.6 in G, to -2.262 in L. Simulations in B, D, I, and J do not correspond to any particular piece of experimental data.

1s2p RIXS simulations as well. Fig. 5, *Top* shows a series of RIXS simulations, starting with the low-spin ferric simulation of Fe3tpp (Fig. 5A). In the Fe3tpp simulation, the energy difference between the LMCT (3d⁶) configuration and the ground (3d⁵) configuration, Δ , is 1.5 eV. As Δ decreases, the weight of the LMCT configuration increases and the wave function gains more ferrous character, becoming 2% 3d⁵ (Fig. 5F). The low-energy $d\pi$ -peak also decreases in intensity and shifts up in energy, eventually merging into the main peak in Fig. 5E.

Fig. 5, *Bottom* shows a series of RIXS simulations, starting with the low-spin ferrous simulation of Fe2tpp on the left. In this series, the energy difference between the LMCT (3d⁵) and ground (3d⁶) configurations, Δ_{bb} , is decreased going from left to right. As the weight of the LMCT configuration increases, the wave function gains more ferric character, and a low-energy $d\pi$ -peak appears in Fig. 5J, which gains in intensity and moves to lower energy. Correlation of these simulations to the HbO₂ data, which have a low-intensity $d\pi$ -peak close in energy to the main peak (Figs. 1 and 2), show that they can be simulated as a mixed wave function of low-spin 3d⁶ and 3d⁵ configurations; thus, qualitatively it can either be described as a low-spin ferric site with strong π -donation into the $d\pi$ -hole, or a low-spin ferrous center with extensive π -backbonding into the O₂.

By fitting the Fe2tpp, pfpO₂, HbO₂, and Fe3tpp data along the Fe^{III} → Fe^{II} (Fig. 5, *Top*) and Fe^{II} → Fe^{III} (Fig. 5, *Bottom*) series, the amount of Fe^{II}/Fe^{III} character in each system can be estimated to obtain a more quantitative description of the electronic structure. The simulated integrated CEE and CIE were compared with the experimental data to find the best match within a series (*SI Appendix*, Figs. S7–S10 and Table S3). Since the VBCI model only calculates quadrupole intensity, it is directly comparable to the pfpO₂, Fe2tpp, and Fe3tpp datasets. However, because the HbO₂ contains some dipole intensity in the main peak, the intensity and energy splitting of the low-energy peak (in both the CIE and CEE) is the primary handle for comparing the VBCI simulations to the experimental data. The Fe2tpp and Fe3tpp fits were used as Fe^{II} and Fe^{III} limits (39), representing 0 and 100% “Fe^{III}” character, respectively. The first limit

corresponds to 2% 3d⁵ character and the second limit to 66% 3d⁵ character. The difference between Fe^{III} and 3d⁵ character comes from ligand donation and backdonation present already in the reference complexes. The Fe^{III} character for pfpO₂ and HbO₂ were then defined relative to those references (*SI Appendix*, *SI VBCI Fitting*). The resulting fits (Fig. 6) show that along the Fe^{III} → Fe^{II} series, pfpO₂ has 6% Fe^{III} character, while HbO₂ has 50% Fe^{III} character. In the Fe^{II} → Fe^{III} series, pfpO₂ has 8% Fe^{III} character, while HbO₂ has 77% Fe^{III} character. Thus, the fitting shows that pfpO₂ is dominantly Fe^{II}, and that HbO₂ has a very mixed Fe^{II}/Fe^{III} wave function that has more Fe^{III} character.

Discussion

From the VBCI modeling of the 1s2p RIXS data, HbO₂ is best described as a polarized mixed Fe^{II}/Fe^{III} system that has 50–77% Fe^{III} character. This contrasts with pfpO₂, which is best described as an unpolarized Fe^{II} with 6–8% Fe^{III} character. The modeling also shows that the difference in electronic structure can be attributed to the covalency of the Fe–O₂ π -bond. HbO₂ has significantly more Fe^{III} character than pfpO₂ because of greater π -backbonding to O₂. These results combined with DFT definitively show the stark difference between HbO₂ and its “good” model, pfpO₂, due to the distal histidine H bond to the O₂ combined with the less hydrophobic protein environment. Both are important in polarizing the Fe–O₂ π -bond. In previous studies on {FeNO}⁶, it was found that the degree of polarization is governed by the magnitude of the energy gap of the Fe–NO π -bonding and antibonding orbitals relative to the strength of the exchange interaction between electrons in these orbitals (44). When the energy gap is large relative to the exchange interaction, the bond remains unpolarized. As the energy gap decreases, the wave function becomes more polarized (*SI Appendix*, Scheme S1).

pfpO₂ thus has a large enough energy gap to result in an unpolarized bonding description. The addition of the H bond and increased dielectric in the protein stabilize the O₂ π^* -orbital energy, which leads to polarization of the Fe–O₂ π -bond and the appearance of a low-energy peak in the RIXS spectrum in Fig. 1C. These electronic structure descriptions, unpolarized Fe^{II} for pfpO₂ and mixed Fe^{II}/Fe^{III} for HbO₂ due to greater π -backbonding into O₂ are consistent with other experimental data. L-edge XAS provided evidence that pfpO₂ is an unpolarized Fe^{II} with moderate backbonding to O₂ (23). The K edge of HbO₂ is shifted slightly higher in energy compared with pfpO₂ (*SI Appendix*, Fig. S2), and both are between Fe2tpp and Fe3tpp, with pfpO₂ closer to Fe2tpp and HbO₂ closer to Fe3tpp. Although previous iron K β measurements on HbO₂ and oxy-myoglobin suggested the iron is S = 1 based on the high intensity of a satellite peak at ~7,045 eV, we have measured the K β

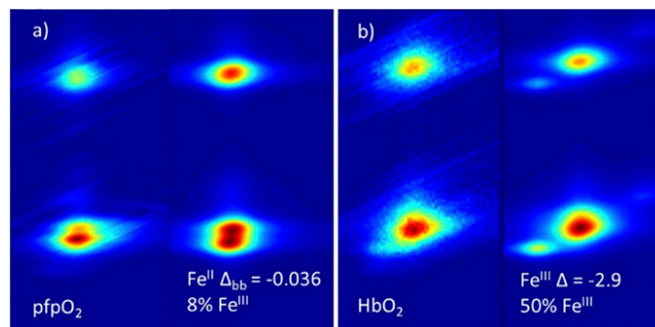


Fig. 6. Best VBCI fits from the simulations described in Fig. 5 for (A) pfpO₂ and (B) HbO₂ with the experimental data on the left, and the fit on the right. Since the results showed that pfpO₂ is dominantly Fe^{II}, the Fe^{II} fit is given. In the case of HbO₂, the results showed a mixed wave function that is more Fe^{III}, and therefore the Fe^{III} fit is given.

spectrum of the HbO₂ sample used here and found a significantly weaker satellite feature that is not consistent with an S = 1 Fe (SI Appendix, Fig. S15) (17). The Fe^{II} S = 1 description of HbO₂ also requires polarized Fe–O π -backbonding and polarized O–Fe σ -donation. Attempts to use the VBCI multiplet model to simulate the experimental RIXS data using this description were unsuccessful. The RIXS analysis is also consistent with previous vibrational and Mössbauer spectroscopic studies. Those methods have been used to describe pfpO₂ and HbO₂ as similar and Fe^{III}. However, alternative interpretations also agree with the X-ray results showing less Fe^{III} character (SI Appendix, Discussion on {FeO₂}⁸ O–O Stretching Frequencies and Mössbauer Parameters).

These results also provide an experimental basis for further calculations. As observed in the previous section, DFT calculations provide a poor description of these oxy-Fe sites. DFT is a single-determinant method and gives ferric descriptions, while the data indicate more ferrous character. Multireference methods, such as complete active space self-consistent field, are best to correlate to these data. Importantly, the experimental data show the H bond and protein environment have a large effect on the {FeO₂}⁸ electronic structure, inducing some polarization in the Fe–O₂ π -bond. These RIXS data on the electronic structure of

oxyhemoglobin and its pfp model should provide the experimental basis for more detailed electronic structure considerations.

Materials and Methods

Oxy-picket-fence porphyrin samples were prepared as described in ref. 31. Hemoglobin samples were prepared as described in ref. 16. K-edge XAS data were collected at beam line 7–3 at the Stanford Synchrotron Radiation Lightsource (SSRL). RIXS data were collected at beam line 6–2 at SSRL and ID-26 at the European Synchrotron Radiation Facility. VBCI modeling was performed using the models developed by Cowan (45) and Thole et al. (46) DFT calculations were performed using the Orca 3.0.3 software package (47). Full details on sample preparation, spectroscopic experiments, and calculations are included in SI Appendix, SI Materials and Methods.

ACKNOWLEDGMENTS. This work was supported by the National Institutes of Health (Grant GM-40392 to E.I.S.). Use of the Stanford Synchrotron Radiation Lightsource (SSRL), SLAC National Accelerator Laboratory, is supported by the US Department of Energy (DOE), Office of Science, Office of Basic Energy Sciences under Contract DE-AC02-76SF00515. The SSRL Structural Molecular Biology Program is supported by the DOE Office of Biological and Environmental Research, and by the National Institutes of Health, National Institute of General Medical Sciences (Grant P41GM103393 to K.O.H and B.H.). T.K. acknowledges financial support by the German Research Foundation (DFG) Grant KR3611/2-1. M.L.B. acknowledges the support of the Human Frontier Science Program. M.L. acknowledges support from the Marcus and Amalia Wallenberg Foundation.

- Enemark JH, Feltham RD (1974) Principles of structure, bonding, and reactivity for metal nitrosyl complexes. *Coord Chem Rev* 13:339–406.
- Pauling L, Coryell CD (1936) The magnetic properties and structure of hemoglobin, oxyhemoglobin and carbonmonoxyhemoglobin. *Proc Natl Acad Sci USA* 22:210–216.
- Pauling L (1964) Nature of the iron-oxygen bond in oxyhaemoglobin. *Nature* 203:182–183.
- Weiss JJ (1964) Nature of the iron-oxygen bond in oxyhaemoglobin. *Nature* 202:83–84.
- McClure DS (1960) Electronic structure of transition-metal complex ions. *Radiat Res Suppl* 2:218–242.
- Harcourt RD (1971) Increased-valence formulae and the bonding of oxygen to haemoglobin. *Int J Quantum Chem* 5:479–495.
- Harcourt RD (1990) Comment on a CASCF study of the Fe–O₂ bond in a dioxygen heme complex. *Chem Phys Lett* 167:374–377.
- Goddard WA, 3rd, Olafson BD (1975) Ozone model for bonding of an O₂ to heme in oxyhemoglobin. *Proc Natl Acad Sci USA* 72:2335–2339.
- Chen H, Ikeda-Saito M, Shaik S (2008) Nature of the Fe–O₂ bonding in oxy-myoglobin: Effect of the protein. *J Am Chem Soc* 130:14778–14790.
- Liao M-S, Huang M-J, Watts JD (2010) Iron porphyrins with different imidazole ligands. A theoretical comparative study. *J Phys Chem A* 114:9554–9569.
- Attia AAA, Lupan A, Silaghi-Dumitrescu R (2013) Spin state preference and bond formation/cleavage barriers in ferrous-dioxygen heme adducts: Remarkable dependence on methodology. *RSC Adv* 3:26194–26204.
- Kepp KP, Dasmeh P (2013) Effect of distal interactions on O₂ binding to heme. *J Phys Chem B* 117:3755–3770.
- Jensen KP, Ryde U (2004) How O₂ binds to heme: Reasons for rapid binding and spin inversion. *J Biol Chem* 279:14561–14569.
- Hocking RK, et al. (2007) Fe L-edge X-ray absorption spectroscopy of low-spin heme relative to non-heme Fe complexes: Delocalization of Fe d-electrons into the porphyrin ligand. *J Am Chem Soc* 129:113–125.
- Bren KL, Eisenberg R, Gray HB (2015) Discovery of the magnetic behavior of hemoglobin: A beginning of bioinorganic chemistry. *Proc Natl Acad Sci USA* 112:13123–13127.
- Wilson SA, et al. (2013) X-ray absorption spectroscopic investigation of the electronic structure differences in solution and crystalline oxyhemoglobin. *Proc Natl Acad Sci USA* 110:16333–16338.
- Schuth N, et al. (2017) Effective intermediate-spin iron in O₂-transporting heme proteins. *Proc Natl Acad Sci USA* 114:8556–8561, and erratum (2017) 114:E8129.
- Wasinger EC, de Groot FMF, Hedman B, Hodgson KO, Solomon EI (2003) L-edge X-ray absorption spectroscopy of non-heme iron sites: Experimental determination of differential orbital covalency. *J Am Chem Soc* 125:12894–12906.
- Baker ML, et al. (2017) K- and L-edge X-ray absorption spectroscopy (XAS) and resonant inelastic X-ray scattering (RIXS) determination of differential orbital covalency (DOC) of transition metal sites. *Coord Chem Rev* 345:182–208.
- Hocking RK, et al. (2009) Fe L- and K-edge XAS of low-spin ferric corrole: Bonding and reactivity relative to low-spin ferric porphyrin. *Inorg Chem* 48:1678–1688.
- Hocking RK, et al. (2010) Fe L-edge X-ray absorption spectroscopy determination of differential orbital covalency of siderophore model compounds: Electronic structure contributions to high stability constants. *J Am Chem Soc* 132:4006–4015.
- Hocking RK, et al. (2006) Fe L-edge XAS studies of K₄[Fe(CN)₆] and K₃[Fe(CN)₆]: A direct probe of back-bonding. *J Am Chem Soc* 128:10442–10451.
- Wilson SA, et al. (2013) Iron L-edge X-ray absorption spectroscopy of oxy-picket fence porphyrin: Experimental insight into Fe–O₂ bonding. *J Am Chem Soc* 135:1124–1136.
- Barlow CH, Maxwell JC, Wallace WJ, Caughey WS (1973) Elucidation of the mode of binding of oxygen to iron in oxyhemoglobin by infrared spectroscopy. *Biochem Biophys Res Commun* 55:91–96.
- Maxwell JC, Volpe JA, Barlow CH, Caughey WS (1974) Infrared evidence for the mode of binding of oxygen to iron of myoglobin from heart muscle. *Biochem Biophys Res Commun* 58:166–171.
- Potter WT, Tucker MP, Houtchens RA, Caughey WS (1987) Oxygen infrared spectra of oxyhemoglobins and oxymyoglobins. Evidence of two major liganded O₂ structures. *Biochemistry* 26:4699–4707.
- Collman JP, Brauman JI, Halbert TR, Suslick KS (1976) Nature of O₂ and CO binding to metalloporphyrins and heme proteins. *Proc Natl Acad Sci USA* 73:3333–3337.
- Tsai TE, Groves JL, Wu CS (1981) Electronic structure of iron–dioxygen bond in oxy-Hb-A and its isolated oxy- α and oxy- β chains. *J Chem Phys* 74:4306–4314.
- Boso B, Debrunner PG, Wagner GC, Inubushi T (1984) High-field, variable-temperature Mössbauer effect measurement on oxyheme proteins. *Biochim Biophys Acta* 791:244–251.
- Oshtrakh MI, et al. (2011) Heme iron state in various oxyhemoglobins probed using Mössbauer spectroscopy with a high velocity resolution. *Biomaterials* 24:501–512.
- Spartalian K, Lang G, Collman JP, Gagne RR, Reed CA (1975) Mössbauer spectroscopy of hemoglobin model compounds: Evidence for conformational excitation. *J Chem Phys* 63:5375–5382.
- Collman JP, et al. (1980) Synthesis and characterization of “tailed picket fence” porphyrins. *J Am Chem Soc* 102:4182–4192.
- Li J, Noll BC, Oliver AG, Schulz CE, Scheidt WR (2013) Correlated ligand dynamics in oxiron picket fence porphyrins: Structural and Mössbauer investigations. *J Am Chem Soc* 135:15627–15641.
- Glatzel P, Bergmann U (2005) High resolution 1s core hole X-ray spectroscopy in 3d transition metal complexes—Electronic and structural information. *Coord Chem Rev* 249:65–95.
- Glatzel P, et al. (2004) The electronic structure of Mn in oxides, coordination complexes, and the oxygen-evolving complex of photosystem II studied by resonant inelastic X-ray scattering. *J Am Chem Soc* 126:9946–9959.
- de Groot FMF, et al. (2005) 1s2p resonant inelastic X-ray scattering of iron oxides. *J Phys Chem B* 109:20751–20762.
- Kroll T, Lundberg M, Solomon EI (2016) *X-Ray Absorption and RIXS on Coordination Complexes. X-Ray Absorption and X-Ray Emission Spectroscopy* (John Wiley & Sons, Chichester, UK), pp 407–435.
- Lundberg M, et al. (2013) Metal-ligand covalency of iron complexes from high-resolution resonant inelastic X-ray scattering. *J Am Chem Soc* 135:17121–17134.
- Kroll T, et al. (2014) Resonant inelastic X-ray scattering on ferrous and ferric bis-imidazole porphyrin and cytochrome c: Nature and role of the axial methionine-Fe bond. *J Am Chem Soc* 136:18087–18099.
- Westre TE, et al. (1997) A multiplet analysis of Fe K-edge 1s → 3d pre-edge features of iron complexes. *J Am Chem Soc* 119:6297–6314.
- Wasinger EC, et al. (2002) X-ray absorption spectroscopic investigation of the resting ferrous and cosubstrate-bound active sites of phenylalanine hydroxylase. *Biochemistry* 41:6211–6217.
- Park S-Y, Yokoyama T, Shibayama N, Shiro Y, Tame JRH (2006) 1.25 Å resolution crystal structures of human haemoglobin in the oxy, deoxy and carbonmonoxy forms. *J Mol Biol* 360:690–701.
- Jameson GB, et al. (1978) Structure of a dioxygen adduct of (1-methylimidazole)-meso-tetrakis(α,α,α -o-pivalamidophenyl)porphyrinatoiron(II). An iron dioxygen model for the heme component of oxymyoglobin. *Inorg Chem* 17:850–857.
- Yan JJ, et al. (2017) L-edge X-ray absorption spectroscopic investigation of FeNO⁶: Delocalization vs antiferromagnetic coupling. *J Am Chem Soc* 139:1215–1225.
- Cowan RD (1981) *The Theory of Atomic Structure and Spectra* (Univ of California Press, Berkeley, CA), p xviii.
- Thole BT, et al. (1985) 3d x-ray-absorption lines and the 3d⁹4fⁿ⁺¹ multiplets of the lanthanides. *Phys Rev B Condens Matter* 32:5107–5118.
- Frank N (2012) The ORCA program system. *Wiley Interdiscip Rev Comput Mol Sci* 2: 73–78.